eTransportation 28 (2026) 100554

Contents lists available at ScienceDirect

eTransportation

journal homepage: www.journals.elsevier.com/etransportation

Visualizing electrolyte dynamics and monitoring salt concentration to improve commercial Si-based Li-ion batteries

Nilanka M. Keppetipola [a,b,e], Clémence Alphen [a,b,e], Marina-Lamprini Vlara [a,b,e], Christoph Stangl [c], Christophe Caucheteur [d], Ozlem Sel [a,b,e], Jean-Marie Tarascon [a,b,e,*]

[a] Chimie du Solide et de L'Energie, UMR, Collège de France, 75231, Paris, France
[b] Réseau sur le Stockage Electrochimique de l'Energie (RS2E), CNRS FR3459, Amiens, 80039, France
[c] VARTA Innovation GmbH, Graz, Styria, Austria
[d] Advanced Photonic Sensors Unit, University of Mons, 31 Boulevard Dolez, 7000 Mons, Belgium
[e] Sorbonne Université–Campus Pierre-et-Marie-Curie, Paris, France

ARTICLE INFO

Keywords:
Li-ion cells
Silicon anode
Solid electrolyte interface
Tilted fiber bragg grating sensor
Volume expansion

ABSTRACT

The race for Li-ion batteries with higher energy density has led researchers toward Si-rich/Carbon composites, though their >200 % volume change induces strong electrolyte dynamics. The challenge is therefore to understand how this electrolyte dynamics contributes to cell formation and degradation under real operating conditions. Herein, we answer this question by combining optical calorimetry, and use of multiplexed tilted fiber Bragg grating sensors (TFBGs), to monitor electrolyte motion and Li-ion concentration gradient within a cell. For proof of concept, we used 21700 cylindrical prototype cells based on either graphite or SiC composite as negative electrode. We found a continuous and irreversible heat generation associated with the solid electrolyte interphase (SEI) formation throughout the entire charging process for SiC, unlike graphite-based cells. In addition, we provided evidence of reversible changes in hydrostatic pressure in SiC cells during cycling, related to the real-time movement of the electrolyte. Interestingly, the concomitant expansion-contraction and electrolyte movement caused depletion and inhomogeneous $LiPF_6$ concentration, with nearly 35 % in the bottom area and 10 % in the middle area of the cell mandrel after 100 cycles. These insights, obtained through *operando* optical detection of cylindrical cells, should be of great help to battery manufacturers in streamlining formation protocols and reducing manufacturing costs.

1. Introduction

Driven by the global trend toward electric transportation, research on lithium-ion batteries is increasingly focused on improving their energy density to meet future demands [1]. One approach is to use the high energy density anode materials such as Silicon (theoretical specific capacity of 4200 mAh g^{-1}) to replace the conventional graphite anodes (372 mAh g^{-1}), which significantly improve the cell capacity [2]. However, several challenges hinder practical implementation - including substantial volume expansion of up to 300 % during the lithiation/delithiation process, continuous growth of the solid electrolyte interphase (SEI), relatively low Li^+ ionic conductivity (ranging from 10^{-5} to 10^{-3} S cm^{-1}) and diffusion (around 10^{-14} to 10^{-13} cm^2 s^{-1}) were observed in Li_xSi [3,4].

In recent years, a variety of methods have been successfully developed to address these challenges. For example, researchers have synthesized Silicon carbon (SiC) nanocomposite anodes to reduce the volume expansion [5,6], engineered electrolyte additive [7,8], incorporated heteroatoms into silicon oxide [9]. However, many of these studies are conducted on small batches of material and electrodes, which limits their applicability to testing in coin cells or single-layer pouch cell formats. Some studies, however, have reported aging mechanisms that do not appear at the laboratory scale but which become evident in large-scale format cells due to the mesoscopic and macroscopic characteristics of cell geometry [10,11]. Besides, multiple reports have shown significant irregularities in lithium plating patterns during

* Corresponding author. Chimie du Solide et de L'Energie, UMR, Collège de France, 75231, Paris, France.
E-mail addresses: nilanka.keppetipola@college-de-france.fr (N.M. Keppetipola), clemence.alphen@college-de-france.fr (C. Alphen), marina.vlara@college-de-france.fr (M.-L. Vlara), Christoph.Stangl@varta-ag.com (C. Stangl), Christophe.CAUCHETEUR@umons.ac.be (C. Caucheteur), ozlem.sel@college-de-france.fr (O. Sel), jean-marie.tarascon@college-de-france.fr (J.-M. Tarascon).

https://doi.org/10.1016/j.etran.2026.100554
Received 13 November 2025; Received in revised form 12 January 2026; Accepted 27 January 2026
Available online 28 January 2026

cycling [12,13]. These inconsistencies are often triggered by variations in temperature, pressure, and the distribution of materials across and along the cell [14,15].

A study conducted by Solchenbach et al. at BMW showed that electrolyte movement plays a critical role in the aging of large-format 4695 cells during repeated fast charging [11], and that the distribution of $LiPF_6$ salt becomes uneven throughout the jelly roll during cycling. Post-mortem analysis revealed higher salt concentrations near the center of the jelly roll and lower towards the edges. Areas with reduced salt levels, especially near the anode, showed signs of lithium plating, likely due to decreased ionic conductivity resulting in local overpotentials.

Recently, Dahn J.R. et al. used synchrotron X-ray computed tomography (SR-CT) to image electrolyte movement during fast charging in two types of 18650 cells, one with a graphite anode and the other with a graphite/SiOx composite anode [10]. The influence of gravity was investigated by orienting the cells both vertically and horizontally. The motion patterns of the electrolyte were then correlated with post-mortem measurements of salt concentration within the jelly roll. These results demonstrate how gravity and cell geometry impact electrolyte dynamics, contributing to inhomogeneous distribution of electrolytes and degrading Li-ion batteries. To investigate these phenomena further, *operando* measurements of temperature, pressure and electrolyte dynamics, together with access to key metrics are particularly valuable for understanding and optimizing the next generation silicon-based Li-ion cells.

Optical sensors now play a crucial role in *operando* battery analysis, enabling real-time tracking of chemical, thermal, and mechanical changes that contribute to enhanced safety, lifetime, and sustainability [16]. In particular, Fiber Bragg Grating (FBG) sensors have been integrated into 18650 and pouch cells to monitor temperature (T), pressure (P), strain (ε) and heat ($\dot{Q}$), and to correlate these variations with the battery's state of charge (SoC) and state of health (SoH) [17–21]. To decouple the internal temperature and pressure, pressure-sensitive microstructured FBG (MOF-FBG) sensors were employed alongside FBG implemented on single mode fiber (SMF-FBG). Moreover, tilted FBG (TFBG) sensors have been employed for *operando* monitoring of electrolyte temperature, refractive index, and turbidity, providing correlations with reaction pathways associated with battery capacity loss [22,23].

In this study, we used *operando* optical sensor technology combining SMF-FBG, MOF-FBG, and TFBG sensors, to analyse the abnormal behaviours observed in NMC622/SiC 21700 cylindrical cells compared to NMC622/graphite cells. Unlike graphite-based cells, we observed continuous and irreversible heat generation associated with the SEI layer formation throughout the entire first charging process for SiC cells. Additionally, cells with a SiC composite anode exhibited reversible variations in hydrostatic pressure during cycling, which were associated with electrolyte movement. This, in turn, led to a non-homogeneous Li^+ concentration in the electrolyte - a crucial parameter for ensuring the long cycling life of SiC cells.

2. Methods

2.1. Cell specifications and preparation

Prototype classical tab-based 21700 dry cells were provided by VARTA Innovation and comprised NMC622/SiC-based cells with nominal capacity of 4.1 Ah and 5 Ah, as well as NMC622/Graphite-based cells with the nominal capacity of 2.6 Ah. The electrolyte consisted of 1 M $LiPF_6$ dissolved in EC:EMC:FEC solvent mixture of either 25:70:5 or 20:70:10 (vol %), where EC, EMC, and FEC are ethylene carbonate, ethyl methyl carbonate, and fluoroethylene carbonate, respectively. Unless noted otherwise, all cells were tested using an electrolyte containing 5 vol% FEC. A higher FEC content (10 vol%) was used only for the electrolyte consumption study and was limited to the 4.1 Ah NMC622/SiC-based cells. Table 1 presents the comparison of the key parameters of the NMC622/SiC-based cells used in the experiments. The only difference between the 4.1 Ah and 5 Ah cells was the cathode coating height while keeping the same areal loading.

2.2. Optical sensor fabrication and integration

Three different types of sensors were used, namely single mode fiber Bragg grating (SMF-FBGs) sensors, FBG sensors inscribed in microstructured optical fiber (MOF-FBG) and tilted fiber Bragg grating (TFBGs) sensors. The properties of each, including their sensitivity, are summarized in Table S1. By using appropriate sensors, temperature and pressure can separately be measured [17]. FBGs can monitor external-internal T, P, ε and RI changes under real battery cycling without interfere to the cell performances [16].

To place the internal SMF-FBG and MOF-FBG sensors, a 0.8 mm diameter hole was drilled at the negative pole of 21700 cells. The hole location was chosen based on the welding point, which serves as a good approximation of the cell's center. The cells were vacuum-dried overnight in an oven at 80 °C, before entering to the Ar-filled glove box with H_2O and O_2 content below 0.1 ppm. Afterwards, the cells were filled with electrolyte; specifically, SiC cells were filled with 7 mL (4.1 Ah) and 7.3 mL (5 Ah), compared with 5 mL for graphite cells, in accordance with the manufacturer's recommendation and supporting literature [24]. This higher fill accounts for SiC anodes' higher porosity and surface area, greater reversible expansion, and increased SEI formation, ensuring sufficient electrolyte uptake, full wetting during swelling, and avoidance of dry regions. Finally, cells were sealed with epoxy glue and cured overnight before the measurements. For the degassing procedure, the sensors were passed through a homemade setup (Fig. S2) and sealed after completing the first formation cycle.

For TFBG sensor integration, 0.8 mm holes were drilled at both the positive and negative poles of the 21700 cells. Then the sensors were carefully aligned through the middle void. Afterwards, the positive side was sealed with the epoxy glue, cured overnight before filling electrolyte through the negative side hole. The first formation cycle was performed while the negative side hole left opened in the Ar-filled glove box. Finally, the cell was sealed, cured overnight, and placed in the climate chamber for further cycles.

2.3. Electrochemical testing protocols

The electrochemical performance was carried out using a BCS-810 or MPG2 potentiostat (Bio-Logic, France) at 25 °C in a temperature-

Table 1
Comparison of the parameters of the NMC622/SiC-based cells used in the experiments.

Positive electrode		
Type	NMC622 (4.1 Ah)	NMC622 (5.0 Ah)
Nominal capacity (Ah)	4.1	5.0
Active material (wt.%)	96.5	96.5
Coating Width (cm)	5.50	6.00
Conductive agent	identical	identical
Binder		
Coating thickness		
length		
Areal loading		
Electrolyte	5 % 1 M $LiPF_6$ in EC:EMC:FEC (25:70:5) 10 % 1 M $LiPF_6$ in EC:EMC:FEC (20:70:10)	5 % 1 M $LiPF_6$ in EC:EMC:FEC (25:70:5)
Negative electrode		
SiC (wt%)	75	
Width (cm)	6.14	

controlled oven (Memmert, accuracy ±0.1 °C). Among the three formation cycles, the first galvanostatic charge-discharge cycle was performed at a C/20 rate within a 2.5–4.2 V voltage window on an open cell to facilitate degassing. The second and third formation cycles were conducted on a sealed cell. Following the formation process, pulse tests were carried out at 0.5C and 1C. After the pulse tests, a control cycle (C/20) was performed, followed by cycling at a C/2 rate for 100 cycles.

2.4. Optical measurements and data processing

For *operando* SMF-FBG and MOF-FBG measurements, the reflected spectra were collected using the HYPERION si255 interrogator (Micron Optics, USA). According to the specifications, the wavelength resolution accuracy is 1 pm. For *operando* TFBG measurements, optical transmission spectra were recorded every 10 s intervals using T100S-HP (EXFO SOLUTIONS) laser connected to a CTP10 optical testing platform in the wavelength range of 1500–1600 nm.

2.5. Calibration procedure

After sensor integration and before starting the formation cycles, thermal calibration was performed to calibrate each sensor. During this

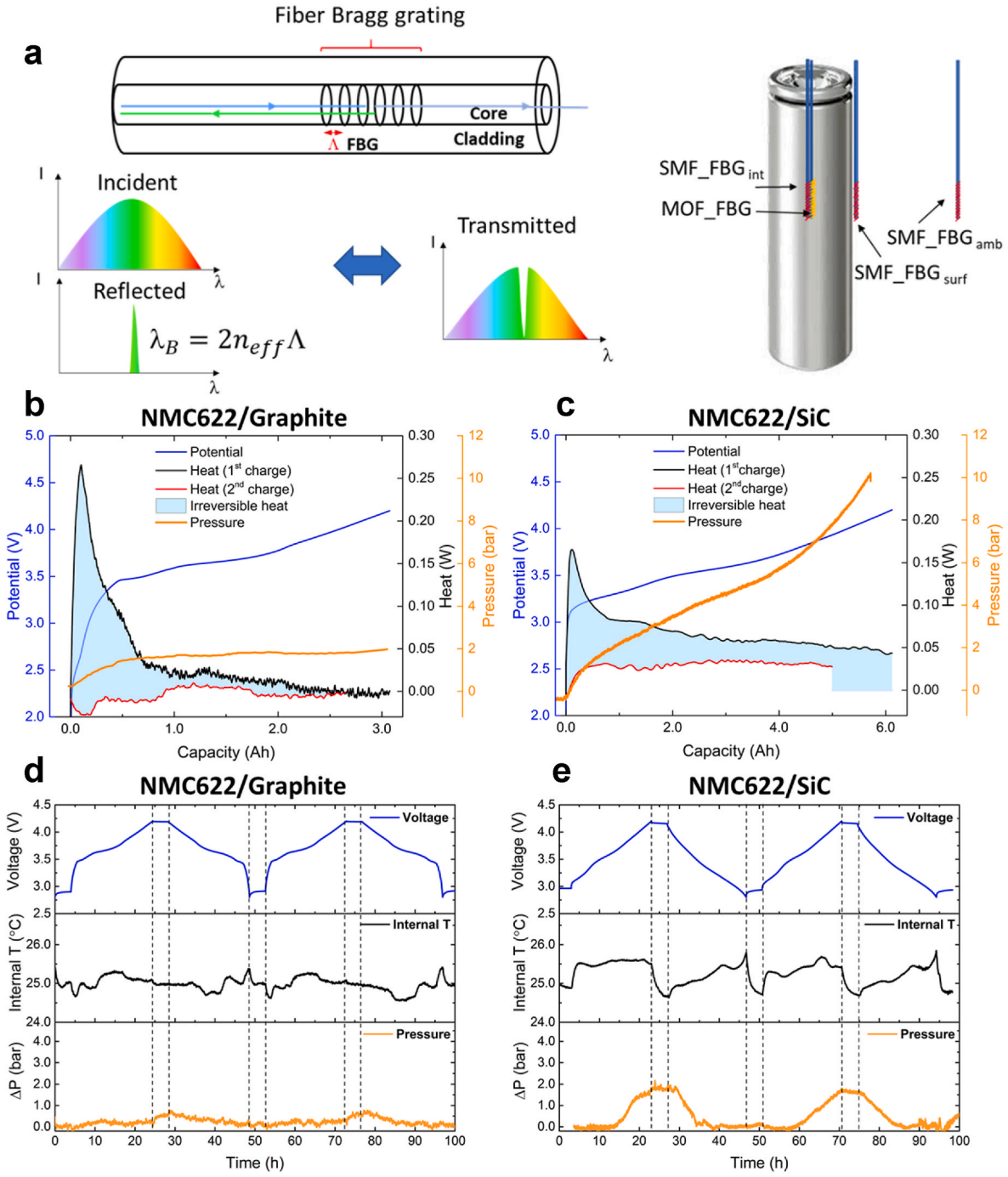

Fig. 1. (a) Working principle of FBG sensor and scheme of the SMF-FBG/MOF-FBG sensors integration in a 21700 cell, (b) and (c) comparison of the temperature and the pressure changes during the first charge of the formation cycle in NMC622/Graphite and NMC622/SiC cell, respectively. (d) and (e) Internal temperature and pressure changes during the subsequent 2nd and 3rd cycle for NMC622/Graphite and NMC622/SiC cell, respectively.

process, the oven temperature was set to 25, 27, 29, 31, and 33 °C, with each temperature maintained for 4 h. This approach allowed for the calculation of the sensitivity coefficients of each sensor, enabling the conversion of wavelength shifts into temperature measurements. The estimated sensitivity coefficients are shown in Table S1. For concentration calibration, measurements began with 3 ml of EC:EMC (3:7) solvent mixture, and a 150 µl of pre-prepared 3 M $LiPF_6$ solution was added stepwise. After that, related cladding peak shifts from TFBG transmission spectra were corrected with the bragg shifts to eliminate the T, P and ε (see Fig. S5a). Finally, sensitivity coefficients were estimated by plotting bragg-corrected wavelength as a function of solution concentration, along with the corresponding linear fit (see Fig. S5b).

2.6. ICP-MS measurements

Li-ion concentration depletion in the electrolyte extracted from the aged cell was quantified using inductively coupled plasma mass spectrometry (ICP-MS; NexION 2000, PerkinElmer). First, the epoxy filling was removed from the aged cell, and electrolyte was ejected through a 0.8 mm hole. A volume of 14 µL of the ejected electrolyte was diluted with 2 wt% nitric acid and made up to a final volume of 100 mL to obtain a Li concentration in the 20–1000 ppb range. The fresh electrolyte sample (1.0 mol dm^{-3} $LiPF_6$ in EC:EMC:FEC = 2.5:7:0.5 v%) was prepared using the same dilution procedure. Calibration solutions were prepared from a lithium ICP standard solution (Sigma-Aldrich, 9981 mg L^{-1} Li) and diluted with 2 wt% nitric acid to concentrations of 20, 50, 100, 200, 300, 500, 700, 800, and 1000 ppb.

3. Results and discussion

FBG sensors inscribed in single-mode fibers (SMF-FBGs) reflect the Bragg wavelength ($\lambda_B = 2n_{eff}\Lambda$), which is sensitive to temperature, strain and slightly to pressure (Fig. 1a), while FBG sensors inscribed in microstructured optical fiber (MOF-FBG) offer greater pressure sensitivity (Table S1). SMF-FBG and MOF-FBG were inserted in cylindrical NMC622/SiC 21700 cells to monitor internal temperature and pressure variations during formation cycles. The results were then compared with those from NMC622/graphite cells (Fig. 1 and S1) for cells charged at a current rate of C/20. For graphite, the temperature rise is more pronounced at the beginning of charging. This is associated with an increase in pressure of up to 2 bars due to electrolyte decomposition during SEI layer formation and subsequent gas formation (Fig. 1b). In contrast, NMC622/SiC cells exhibit consistently higher temperatures throughout the first charge, alongside a much more significant pressure increase of up to 10 bars, primarily driven by gas release during SEI formation (Fig. 1c). The expansion of silicon anodes amplifies this effect, inducing mechanical stress and cracks and causing additional electrolyte degradation as well as further SEI formation [25]. Furthermore, we frequently observed that the performing formation cycle (at C/20) on sealed device leads to a significant increase in pressure, which triggers the Current Interrupt Device (CID) at around 4.1 V, rendering the cell inoperable (Fig. S2a). To address this issue, we have designed a special setup (Fig. S2b) that enables simultaneous sensor integration and controlled degassing during the first formation cycle. This involves connecting the cell to a balloon to collect the gas released during the first formation cycle. Once this is complete, the connection is cut and sealed, allowing the cell to continue operating while optical fiber detection continues. Moreover, the CID break measured at approximately at 10 bars (expected range 10–12 bar) indicates that epoxy applied around the drilled hole provides an effective sealing for the cell during measurements. Additionally, Fig. S2a demonstrates no detectable effect on the electrochemical response between drilled and undrilled cells. These observations are consistent with previous reports that FBG sensors do not alter cell chemistry [17].

The heat released during SEI formation, as calculated from the first and second cycles using optical calorimetry, is 4853 J for the silicon-based cell and 2712 J for the graphite cell. However, it should be noted that these values are not actually that different when expressed in J Ah^{-1}, as the capacity of silicon-based cells (5 Ah) is twice that of graphite-based cells (2.6 Ah). Fig. 1e shows the temperature and pressure profiles of the NMC622/SiC cells during the second and third cycles. Exothermic events of weak amplitude related to subtle Li-driven structural changes occur during charging and discharging [26], with a notable increase in hydrostatic pressure halfway through charging. This continues until the end of charging, after which it stabilizes during the relaxation phase prior to converting back to its initial value at the end of discharge. These reversible changes in hydrostatic pressure most likely mirror electrolyte motion during cycling and are primarily driven by the well-known expansion and contraction of silicon.

When comparing the second and third cycles, graphite-only cells exhibit only a slight, fully reversible pressure change (Fig. 1d), suggesting minimal electrolyte displacement or bulk volume change. In contrast, SiC-containing electrodes show a more pronounced, reversible pressure rise that is consistent with electrode volumetric expansion. While direct observation of electrolyte motion is not available, these reversible pressure changes in SiC-based cells may reflect transient electrolyte-level variations. Such effects appear negligible in graphite-only cells, in line with previous computed-tomography studies of 18650 graphite and SiC-based electrodes, which report limited electrolyte movement in purely graphite anodes [10]. Accordingly, electrolyte-level measurements in this work are presented only for SiC-based cells.

To check for electrolyte movement inside cells, we used multiplexed Tilted Fiber Bragg Grating (TFBG) sensors. In addition to being sensitive to T, P and ε due to Bragg resonance (see Table S1), these sensors are also sensitive to variations in the refractive index (RI) of the media surrounding the fiber via resonance peaks in the cladding modes (see Fig. S3a for TFBG spectra). Thus, by correcting the shifts of the cladding peaks for the temperature, pressure and dielectric constant effects, we can determine changes in RI with high precision (~3000 pm/RIU). To provide a simple proof of concept, a 0.9 cm TFBG sensor was placed in an 18650-cell casing, which was then progressively filled while the sensor spectra were monitored. As shown in Fig. S3b and S3c, the cladding peak intensity decreased and shifted towards a longer wavelength as the electrolyte was added, and the reverse happened when the electrolyte was removed. This shift towards longer wavelengths (redshift) is simply due to an increase in the effective refractive index ($n_{clad,eff}$) of the cladding, since the electrolyte has a higher RI than air (in air 1 and ~1.39). Additionally, the maximum peak intensity decreases, and the sensor detects two low-intensity peaks when the cell is halfway full. This indicates independent coupling and transmission of light from the gas phase and the electrolyte. Overall, these results demonstrate the effectiveness of using TFBG to monitor electrolyte levels in a cell and prompt analysis of changes in electrolyte levels over the approximate 6 cm length of the 21700 battery.

To achieve this, three TFBG sensors were inscribed in a single SMF fiber, spaced 1.4 cm apart, with each grating measuring 0.9 cm in length. Each grating period exhibited a slight variation in grating periods, causing the bragg and the cladding-mode spectra to appear in distinct wavelength regions (Fig. 2a). Moreover, each sensor responds independently, sensing only its local 0.9 cm segment without interference from the others. The sensors were positioned along the central void of the jelly-roll in a 4.1 Ah 21700 NMC622/SiC cell, which was filled with 7 mL of EC:EMC:FEC (25:70:5 vol%) electrolyte (Fig. 2b).

Fig. 2c shows the TFBG responses of the top, middle and bottom sensors recorded at multiple time intervals while the cell is being charged/discharged (Fig. 2d) during the first formation cycle. The spectral response confirms that, after resting, the bottom sensor is fully immersed in the electrolyte, while the top sensors remain above the electrolyte level. Additionally, the relatively low insertion loss observed in the middle sensor suggests partial immersion of its edge in the electrolyte (as observed in Fig. S3). Interestingly, nearly 4 h after the

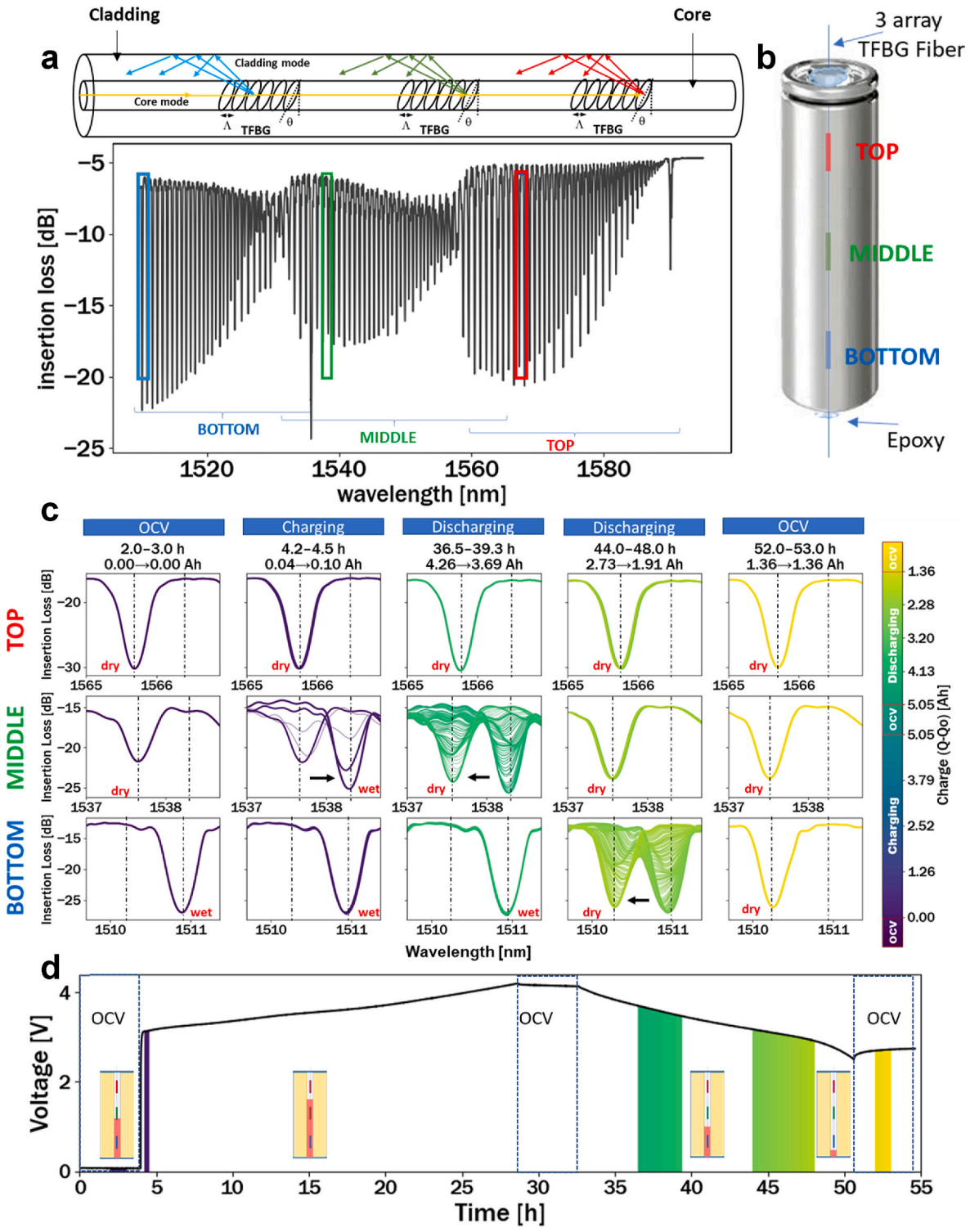

Fig. 2. (a) Schematic of the 3-array TFBG sensor and its transmission spectral response, (b) schematic representation of a TFBG sensor placed and sealed into a 21700 cylindrical cell, (c) evolution of selected cladding mode peaks during the first charge and discharge cycle at C/20 for the 21700 NMC622/SiC 4.1 Ah. cell (Vertical lines indicate the "dry" and "wet" wavelength positions, and arrows show the direction of spectral shift), and (d) Voltage *vs.* time curve for the same cycle. Highlighted regions correspond to the spectral changes shown in (c), with the same color code. Approximate electrolyte levels are shown schematically at each step.

formation cycle started, a gradual modification of the middle sensor's transmission spectra was observed, reminiscent of its progressive immersion into the electrolyte. This observation is most likely the result of SEI growth and the Li-driven expansion of the SiC composite electrode, which exerts pressure on the electrode and forces electrolyte out of the Si electrode [27,28]. This hypothesis was confirmed by discharging the cell and observing a reversible response in the middle sensor, whose spectrum shifted toward lower wavelength and reach a higher insertion loss than before charging. This indicates that the sensor, which was previously partially immersed before charging, is now fully above the electrolyte, revealing a net decrease in electrolyte level after only one cycle. Similarly, the bottom sensor exhibits a shift toward lower wavelength,

indicating that it is now positioned above the electrolyte level. (see 36.5–39.3 and 44–48 h in Fig. 2c).

Overall, this implies that significant amount of electrolyte was consumed during the SEI formation, besides the fact that an indefinite portion may have evaporated (through less than 0.8 mm hole) since the cell was not sealed for this test to prevent CID triggering. This could also explain why the electrolyte did not reach the top sensor after the middle sensor was gradually immersed, despite the continuous expansion of SiC pushing the electrolyte level upwards.

Following the formation cycles, however the cell was sealed after which further control cycles were performed at C/20 while changes in the transmission spectra of the bottom, middle and top TFBGs were mentioned (Fig. 3a). As shown in Fig. 3a, the initial independent coupling and transmission of light from both gas phase and the electrolyte occurred after 2–3 h. This suggests that the electrolyte level rises slightly during the rest period after the first cycle, partially submerging the bottom sensor. This is likely due to gravitational redistribution.

During charging, only the bottom TFBG exhibits a change in its transmission spectrum, which indicates complete immersion in the electrolyte from 30 % SoC onwards. Beyond this point, the transmission spectrum remains unchanged until the end of the charging process. During discharge, this phenomenon appears fully reversible, and the bottom TFBG signal returns to its initial state, matching the spectrum observed prior to charging. (Fig. 3a, bottom sensor 46–47 h and 2–3 h, respectively). This shows that after the formation cycles, the amount of electrolyte consumed is very low. This indicates that the most of the SEI layer has already formed, which is consistent with our optical calorimetry measurements (Fig. 1c and S1c).

Tracking electrolyte consumption during critical SEI formation step is a key factor for cell optimization and our optical sensing data provides direct insight to this process. To further validate electrolyte level changes during this SEI-formation step, we compared two electrolyte formulations that differ in FEC content: EC:EMC:FEC (20:70:10 vol%) and EC:EMC:FEC (25:70:5 vol%). Each cell was filled with 7.0 mL of electrolyte. These formulations were chosen because their differences in FEC contents are known to influence SEI formation behaviour and electrolyte consumption, and thereby providing a sensitive test of our electrolyte-level measurements [29]. Interestingly, as shown in Fig. 3b, in the cell containing 10 % FEC under control cycle at C/20, the bottom sensor was only slightly immersed in the electrolyte at 100 % SOC, and this occurred again during subsequent discharging. The data indicate that the electrolyte level reaches the bottom sensor only at full charge, which corresponds to the cell's maximum expansion. At lower SoC, the electrolyte level lies below the bottom sensor, with most of the electrolyte retained within the jelly roll. These results confirm that the electrolyte containing 10 % FEC undergoes greater degradation, consuming a larger volume of electrolyte to form the SEI compared to the electrolyte containing 5 % FEC electrolyte, as shown by the TFBG sensors. Since FEC is preferentially reduced during the formation cycle to form LiF rich SEI, increasing its concentration results in further additives decomposition, consuming additional Li and thereby lowering the initial coulombic efficiency [7,29,30]. This observation is consistent with Fig. S4, which represents lower first-cycle coulombic efficiency for the 10 % FEC cells (71.9 %) compared to the 5 % FEC cells (73.5 %).

Previous reports have indicated that electrolyte movement in the jelly roll of cylindrical cells can cause significant variations in the lithium ion (Li^+) concentration throughout the cell [11]. At this point, it was therefore reasonable to ask whether these changes, which affect the electrolyte's refractive index, could be detected using TFBGs. With this in mind, we studied the spectral evolution of the cladding modes of a single TFBG sensor under various $LiPF_6$ electrolyte concentrations. $LiPF_6$ concentrations ranging from 0 to 1.4 M in EC:EMC (3:7 v/v) were selected for calibration purposes, and the corresponding sensitivity coefficients were determined via linear regression analysis. As shown in Fig. S5a, the shifts in the cladding peak at each calibrated concentration were corrected using the Bragg shift in order to eliminate any contribution other than changes in the refractive index (i.e. T, P and ε). Finally, we found that the sensitivity coefficient was found to be −40.0 pm/mol dm^{-3} (see Fig. S5b).

Furthermore, we investigated the ability of the multiplexed TFBG sensors to detect salt concentration gradients in the $LiPF_6$-containing electrolyte. Prior to this, the sensitivity coefficients were found to be −29.5 pm/mol dm^{-3}, -38.0 pm/mol dm^{-3} and -27.9 pm/mol dm^{-3} for $LiPF_6$ concentration for the left, middle and right sensors, respectively (see Fig. S6). Fig. S7a illustrates the experimental configuration, wherein the three-sensor TFBG array was inserted through a horizontal needle with two vertical syringes connected to permit the flow of solution. The test was initiated by adding a pre-prepared 3 M $LiPF_6$ solution in EC:EMC (3:7) to one side that already contained a stabilized level of EC:EMC (3:7) solvent mixture. This setup allowed the concentrated solution to flow and diffuse through the needle. The cladding peak shifts were continuously monitored. As shown in Fig. S7b, the cladding peak wavelength shifted progressively along the array as the $LiPF_6$ concentration increased. Fig. S7c shows the calculated concentration changes at each sensor based on the wavelength shift and their respective sensitivity coefficient. After 10 min, distinct concentrations had been detected by each TFBG sensor, forming a measurable concentration gradient that disappeared after 20 min. These results demonstrate the ability of cascaded TFBG sensors to measure concentration gradients at a spacing of 6 cm.

These experiments can only be carried out when the TFBG remains fully immersed in the electrolyte, regardless of the state of charge or discharge of the cell. In the 4.1 Ah cells used to study electrolyte dynamics, full immersion of the bottom sensor was only observed during cycling above a certain SoC in cells containing 5 % FEC electrolyte. The limited immersion makes it challenging to analyse the concentration gradient across the cell using TFBG sensors. To address this, 21700 NMC622/SiC cells with a higher 5 Ah capacity were used, containing 7.3 mL of 1 M $LiPF_6$ in EC:EMC:FEC (25:70:5). As shown by the key cell parameters in Table 1, the only difference between the cells is the wider coated area of the 5 Ah NMC622 electrode (6.0 cm vs. 5.5 cm), with identical areal loading; the SiC content remains unchanged. We therefore expected the 5.0 Ah cells to undergo greater electrode expansion and, as a result, a more pronounced electrolyte rises along the central void compared with the 4.1 Ah cells.

During the formation cycle of the 5 Ah cell, the electrolyte rose to cover all the sensors during the charging and then expanded significantly due to the expansion of the SiC composite anode resulting in the electrolyte being expelled through the degassing outlet (Fig. S8). The displaced electrolyte was collected in an attached syringe and flowed back into the cell during discharge. As shown in Fig. 4a and b, the control cycle (at C/20) performed on the sealed cell produced distinct changes in the transmission spectra monitored by the bottom and middle sensor. Prior to cycling, the bottom sensor was only partially filled (1–3 h) as indicated by its independent coupling and transmission of light. However, by the end of charging, both the bottom and middle sensors were progressively fully immersed. This change is reversible, as the discharge overlaps the initial level (Figs. 4a and 48.5–50.5 h). As the only difference between the 4.1 Ah and 5 Ah is the increased height of the cathode (55 mm and 60 mm, respectively), this supports the conclusion that the 5 Ah SiC cells exhibit comparatively greater volume expansion than the 4.1 Ah cells analyzed earlier (Figs. 2 and 3).

Fig. 4c shows how the insertion loss of the selected cladding peak of the bottom sensor changes alongside the voltage profile, during the first 100 cycles. The cell was cycled at C/2, with a 4 h rest period after every ten cycles. During the initial C/2 cycles, the bottom and middle sensors are completely filled with electrolyte during charging, and this process is then reversed during discharging (see Fig. 4d, left). However, as shown in Fig. 4d (right), continued cycling causes the electrolyte level to slowly and irreversibly rise, most likely due to the permanent expansion of the silicon anode displacing the electrolyte upwards. These results are robust, having been repeated for two different cells.

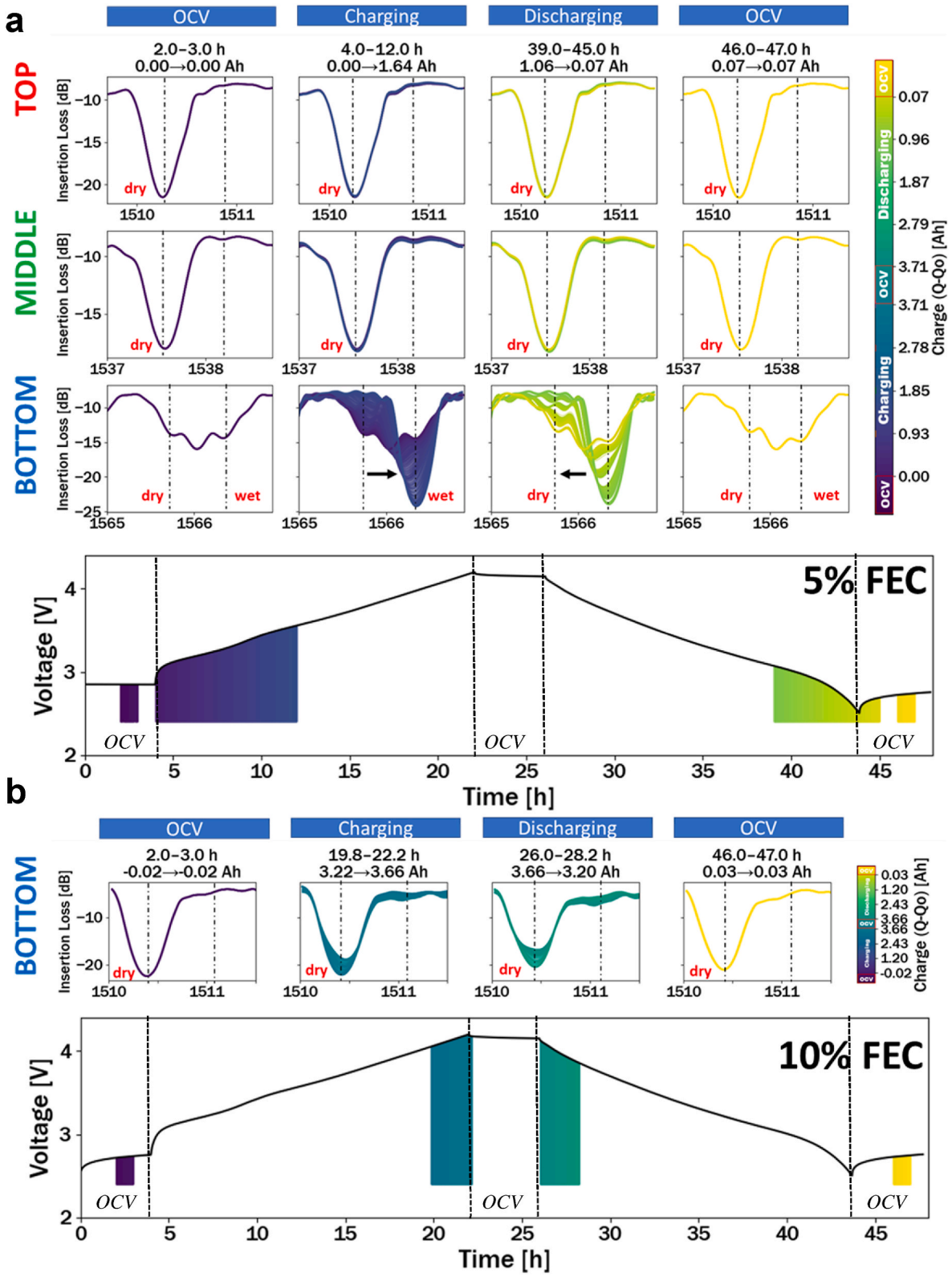

Fig. 3. Evolution of the cladding peaks for 21700 NMC622/SiC cells of 4.1 Ah. (a) Cell with electrolyte containing 5 % FEC showing top, middle and bottom sensors during the control cycle at C/20, along with the voltage *vs.* time curve for the same cycle and (b) cell with electrolyte containing 10 % FEC, showing bottom sensor during the control cycle at C/20, and related voltage *vs.* time curve for the same cycle. Highlighted regions correspond to the spectral changes over the selected time intervals, using the same color code. Vertical lines indicate the "dry" and "wet" wavelength positions, and arrows show the direction of spectral shift.

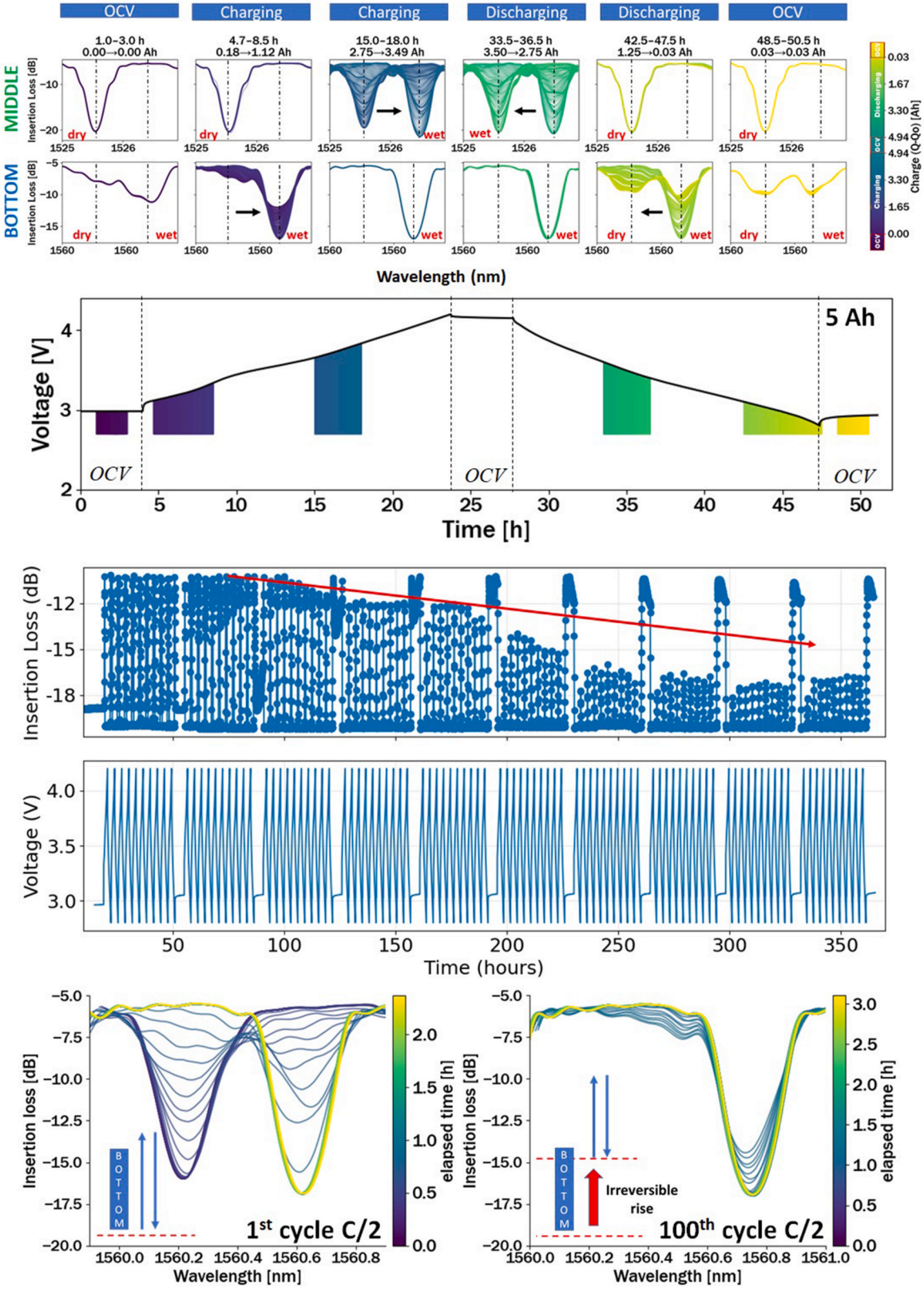

Fig. 4. (a) Evolution of the cladding peaks for middle and bottom sensors during the control cycle at C/20 for 21700 NMC622/SiC cells with 5 Ah capacity (Vertical lines indicate the "dry" and "wet" wavelength positions, and arrows show the direction of spectral shift), (b) Voltage *vs.* time curve for the same cycle. Highlighted regions correspond to the spectral changes shown relative to the voltage profile of the cell. (c) Comparison of the insertion loss of the selected cladding mode peaks during the first 100 cycles, and (d) related cladding mode peak changes of 1st and the 100th cycle.

As mentioned earlier, fully immersing the sensors during cycling enables us to extract additional information, such as changes in the concentration of the $LiPF_6$ electrolyte. This affects the refractive index (RI) of the electrolyte, and we can analyse changes in the wavelength of the TFBG sensors to detect these variations. Indeed, $\Delta\lambda_{TFBG}$ of TFBG cladding mode is the sum of the $\Delta\lambda_{FBG}$, which accounts for the overall contributions of T, P and ε plus $\Delta\lambda_{RI}$ related to RI. However, subtracting $\Delta\lambda_{FBG}$ from $\Delta\lambda_{TFBG}$ simply yields $\Delta\lambda_{RI}$ [22]. However, RI is a temperature-dependent variable that can change from 35 to 40 °C upon cycling (see Fig. 5a). Therefore, we need to calibrate the temperature dependence of the TFBG in our electrolyte. We found refractive index coefficients of −3.37 and −2.12 pm $°C^{-1}$ for the middle and bottom sensors, respectively (see Fig. S9a and S9b). Fig. 5 shows the wavelength changes of the middle and bottom sensors before and after corrections, alongside the capacity change over time. The data were analyzed by taking the average of the corrected wavelengths at the end of the charge and the beginning of the discharge for each cycle (the grey shaded area in Fig. 5). This was then converted to concentrations by taking the initial concentration as 1 M $LiPF_6$ (using the coefficients calculated in Fig. S10). Obviously, this data analysis can only be performed when both sensors are submerged (shaded area in Fig. 5), i.e., when the cell capacity exceeds 3000 mAh.

It is worth noting that the electrolyte used in the 5 Ah cells was EC:EMC:FEC (25:70:5 v%), while the calibration measurements were carried out in EC:EMC (30:70 v%). The concentration analysis was performed after three formation cycles, by which time most of the initially added FEC is expected to have been consumed, as FEC is preferentially reduced during the early formation cycles [29]. This aligns with the low first-cycle coulombic efficiency (~80.6 %) and the large irreversible capacity (~1.2 Ah) observed in Fig. S8, both of which indicate substantial irreversible consumption of reducible species such as FEC.

Fig. 6 shows the estimated change in salt concentration for the middle and bottom sensors during the first 100 cycles. Interestingly, both sensors showed a reduction in Li-ion concentration of around 10–20 % after around 40 cycles. Notably, this value continues to decrease over the cycles, albeit not uniformly. After around 100 cycles, a reduction in Li-ion concentration of 35 % and 10 % is observed for the lower and central sensors, respectively. This difference is significant and robust, given that values of ±5 % were obtained from three cells from the same batch. As the capacity of the cells decays by no more than 9 % after 100 cycles, these large variations in Li-ion concentration cannot be solely attributed to lithium (Li) losses due to parasitic reactions. Rather, they suggest the formation of electrolyte gradients during cycling caused by the repeated contraction and expansion of silicon (Si) in the negative electrode, resulting in electrolyte movement within the cell.

For further validate the Li-ion concentration changes measured by the TFBG sensors, we carried out ICP-MS analysis on electrolyte extracted from aged cells. Fig. S11 shows the calibration curve and the determination of the Li ion concentration relative to fresh electrolyte (1.0 mol dm^{-3}) as reference. The aged electrolyte shows a clear reduction of ~14 % in Li ion centration (0.86 mol dm^{-3}). This value falls within the range analyzed by the TFBG measurements (~10 % depletion near mid-cell and ~35 % near the bottom), supporting depletion of Li-ion concentration during cycling in the central void. During ejection

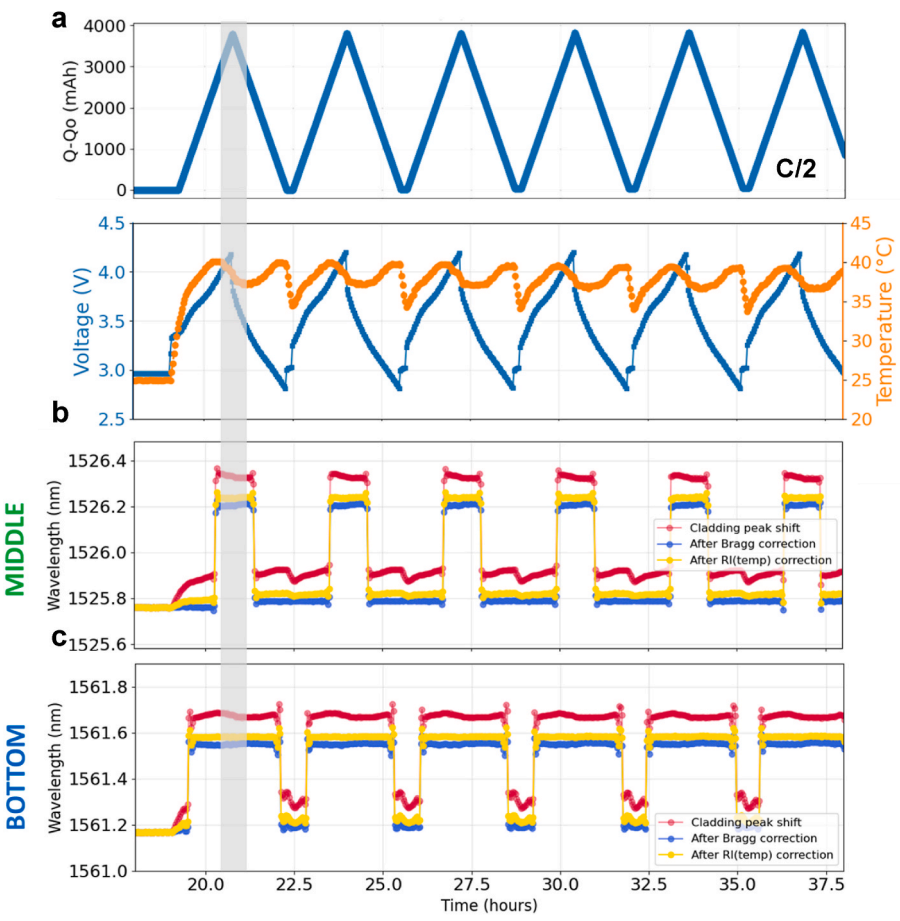

Fig. 5. (a) Capacity change and voltage *versus* time for 5 Ah cell at C/2 cycling rate and related internal temperature change analyzed by Bragg peak shifts. Wavelength shifts of cladding peaks (red), after Bragg correction (blue), and after RI correction (in response to temperature changes) (yellow) for (b) the middle sensor and (c) the bottom sensor. The shaded area indicates the period during the first cycle when both sensors were immersed inside the cell; the average wavelength at each cycle was used to estimate the concentration change.

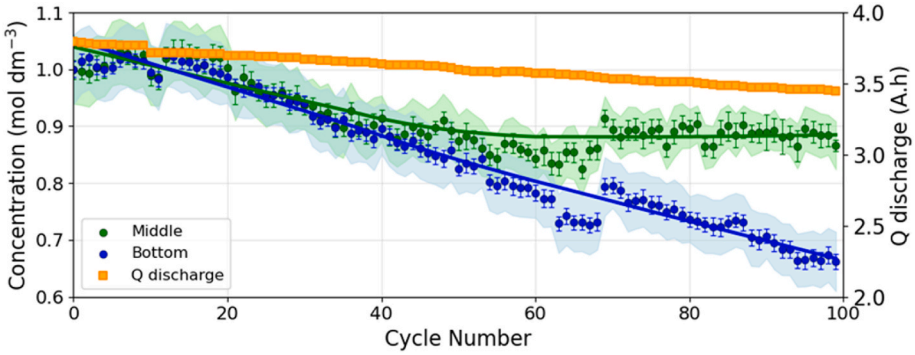

Fig. 6. Estimated $LiPF_6$ concentration at the central void versus cycle number for the middle (green) and bottom (blue), and discharged capacity (orange) versus cycle number of a 5 Ah NMC622/SiC 21700 cells. Markers are cycle-averaged concentrations calculated from the mean corrected wavelength in each cycle. Error bars show the standard error of the mean for the concentration averaging. The shaded bands indicate the ±1σ temperature-driven concentration uncertainty (temperature variability estimated from Bragg shifts) before RI (temp) correction.

through the 0.8 mm hole, electrolyte that had moved to the interlayer may have remixed with electrolyte at the central mandrel, potentially affecting the measured concentration.

This corroborates the conclusions of a recent study by Solchenbach et al. [11], in which the authors observed a $LiPF_6$ concentration gradient in 4695 NMC/SiGr cells and attributed this to electrolyte movement. More specifically, they claim that during charge, the electrolyte is pumped out of the 'jelly roll' towards the empty central region, resulting in $LiPF_6$ depletion, explaining the lower Li^+ content (0.8 versus 1 M) detected by our TFBG sensors in the central region of the cell. However, during discharge, the $LiPF_6$-depleted electrolyte from the central void flows back to the 'jelly roll'. Repeating this process over multiple cycles results in a gradual decrease in Li^+ concentration within the central void, as well as the development of a Li^+ concentration gradient along the cell's Y-axis. This is in line with what we observed using TFBG sensors.

Overall, the electrolyte dynamics associated with Si-based cells during cycling lead to a pronounced Li^+ depletion in the central void of the cell during the first tens of cycles (Fig. 6) after which with this depletion becomes more pronounced at the bottom rather than at the middle of the central void. At this stage, to better understand the formation of electrolyte concentration gradients in the jelly roll of cylindrical cells, *in-situ* measurements should be conducted by placing TFBG sensors across the interlayers of the jelly roll while monitoring the electrolyte concentration in the central void. This is the objective of our ongoing research.

Finally, we believe that these findings, which include *operando* monitoring of heat generation, pressure evolution, electrolyte dynamics, and concentration tracking, will provide valuable guidance for optimizing manufacturing protocols. Real-time identification of SEI-related thermal and pressure signatures provides a basis for adjusting early-stage charging currents, step durations, and additive content to moderate SEI growth and limit irreversible electrolyte consumption, as evidenced by the distinct behaviors observed for electrolytes containing additives. Pressure feedback, together with electrolyte movements, further offers a pathway to guide gas venting strategies and electrolyte volume decisions, particularly in high-capacity cells where both reversible and irreversible pressure components influence cycling stability. Moreover, access to coupled thermal, mechanical, and electrolyte concentration data provides extra additional control parameters that can greatly help with the rational balancing of formation efficiency, electrolyte utilization, and long-term performance although this study does not yet quantify values of specific gains in formation time or material savings. This capability is especially relevant for SiC-based commercial cells, which exhibit elevated electrolyte consumption and redistribution during formation, and more broadly provides a scalable diagnostic framework for data-driven optimization of formation protocols across advanced lithium-ion cell chemistries.

4. Conclusion

We have reported on the *operando* use of optical sensors to elucidate the origin of the different behaviors observed during the formation and aging cycles in 21700 cells with either NMC622/SiC or NMC622/graphite chemistries. Using optical calorimetry, we first observed continuous and irreversible heat generation associated with the SEI layer in SiC based cells throughout the entire charging process. This contrasts with graphite-based cells, where it only occurs at the start of charging. Furthermore, we demonstrate that, unlike graphite-based cells, silicon-based cells accumulate high hydrostatic pressure during the formation cycle. This can cause the safety valve to open during this cycle. It explains why a two-step charging process is currently used to activate cells with a negative electrode containing high levels of silicon. Moreover, in contrast to graphite cells, Si-based cells experienced substantial reversible hydrostatic pressure changes during continuous cycling, associated with electrolyte movement. These changes were visualized in real time using multiplexed TFBG sensors.

We also monitored the electrolyte consumption during the SEI formation in electrolytes containing 5 % and 10 % FEC. Based on electrolyte movements we observed comparatively greater consumption in the 10 % FEC electrolyte. Furthermore, we found that the expansion and contraction of the SiC electrode leads to electrolyte movement and an inhomogeneous Li^+ concentration. After 100 cycles, we found that the Li^+ concentration was nearly 35 % in the bottom area and 10 % in the middle area of the central void of the jelly roll. These observations suggest that a Li^+ concentration gradient is forming within the central void. This is consistent with the formation mechanism of concentration gradients proposed by Solchenbach et al. [11]. Clearly, the degree of electrolyte movement depends on the electrolyte content of the cell (low or high), with the latter having a higher Li^+ content gradient and poorer capacity retention. Therefore, it is critical to find the optimal amount of electrolyte, tailored to the jellyroll dimensions (18650, 21750 or 46800), the silicon (Si) content of the SiC composite electrodes and the available free pore volume which depends on electrode density and porosity [11]. Traditional experimental observations of electrolyte amounts rely largely on trial and error. Although this approach differs from conventional methods, we believe that it will be of great interest to the battery industry. It involves rapidly measuring heat and pressure during cell formation, monitoring the dynamic movement of the electrolyte during cycling, and monitoring the concentration of the Li^+ gradient on commercial cells under practical conditions. If we can make it more user-friendly in terms of fiber injection and data analysis, this approach involving FBGs and TFBGs could provide key metrics for controlling electrolyte quantities in the next generation of silicon-based

Li-ion cells. Collectively, the methodology described here offers a scalable solution for rapidly identifying the best formation processes for commercial cells. We hope that battery manufacturers will take advantage of it.

CRediT authorship contribution statement

Nilanka M. Keppetipola: Writing – review & editing, Writing – original draft, Methodology, Investigation, Formal analysis, Data curation, Conceptualization. **Clémence Alphen:** Writing – review & editing, Methodology. **Marina-Lamprini Vlara:** Writing – review & editing, Methodology. **Christoph Stangl:** Writing – review & editing. **Christophe Caucheteur:** Writing – review & editing. **Ozlem Sel:** Writing – review & editing, Validation, Supervision, Resources, Project administration, Methodology, Funding acquisition. **Jean-Marie Tarascon:** Writing – review & editing, Validation, Supervision, Resources, Project administration, Methodology, Funding acquisition, Conceptualization.

Funding sources

This work was supported by the European Project AccCellBaT "Accelerated Cell and Battery Testing" (European Union's Horizon 2022 research and innovation program under grant agreement No 101103628).

Declaration of competing interest

The authors declare the following financial interests/personal relationships which may be considered as potential competing interests: Jean-Marie Tarascon reports financial support was provided by European Union. If there are other authors, they declare that they have no known competing financial interests or personal relationships that could have appeared to influence the work reported in this paper.

Acknowledgement

N.M. Keppetipola, O. Sel and J.M. Tarascon acknowledge the European Project AccCellBaT "Accelerated Cell and Battery Testing" (European Union's Horizon 2022 research and innovation program under grant agreement No 101103628). We thank Dr. A.Gen Li for his assistance of data analysis scripts. we also gratefully thank Mr. K. Diego, Dr. T. Safarik, Dr. S. Mariyappan, and Dr. C. Gervillié-Mouravieff for their extensive and valuable discussion and comments.

Appendix A. Supplementary data

Supplementary data to this article can be found online at https://doi.org/10.1016/j.etran.2026.100554.

Data availability

Data will be made available on request.

References

[1] Niu H, Zhang N, Lu Y, Zhang Z, Li M, Liu J, et al. Strategies toward the development of high-energy-density lithium batteries. J Energy Storage 2024;88:111666.
[2] Feyzi E, M RAK, Li X, Deng S, Nanda J, Zaghib K. A comprehensive review of silicon anodes for high-energy lithium-ion batteries: challenges, latest developments, and perspectives. Next Energy 2024;5:100176.
[3] Qin T, Yang H, Li Q, Yu X, Li H. Design of functional binders for high-specific-energy lithium-ion batteries: from molecular structure to electrode properties. Industrial Chemistry & Materials 2024;2:191–225.
[4] Farhan G, Toki I, Khalid Hossain M, Rehman WU, Zafar R, Manj A, et al. Recent progress and challenges in silicon-based anode materials for lithium-ion batteries. Industrial Chemistry & Materials 2024;2:226–69.
[5] Ngo DT, Le HTT, Pham XM, Park CN, Park CJ. Facile synthesis of si@sic composite as an anode material for lithium-ion batteries. ACS Appl Mater Interfaces 2017;9:32790–800.
[6] Zhang J, Tang J, Zhou X, Jia M, Ren Y, Jiang M, et al. Optimized porous Si/SiC composite spheres as high-performance anode material for lithium-ion batteries. Chemelectrochem 2019;6:450–5.
[7] Veith GM, Doucet M, Sacci RL, Vacaliuc B, Baldwin JK, Browning JF. Determination of the solid electrolyte interphase structure grown on a silicon electrode using a fluoroethylene carbonate additive. Sci Rep 2017;7:1–15.
[8] Wang J, Li S, Zhang J, Song L, Dong H, Zhang N, et al. Improving toleration of volume expansion of silicon-based anode by constructing a flexible solid-electrolyte interface film via lithium Difluoro(bisoxalato) phosphate electrolyte additive. ACS Sustain Chem Eng 2022;10:15199–210.
[9] Kim T, Li H, Gervasone R, Kim JM, Lee JY. Review on improving the performance of SiOx anodes for a lithium-ion battery through insertion of heteroatoms: state of the art and outlook. Energy Fuels 2023;37:13563–78.
[10] Bond T, Gasilov S, Dressler R, Petibon R, Hy S, Dahn JR. Operando 3D imaging of electrolyte motion in cylindrical Li-Ion cells. J Electrochem Soc 2025;172:030512.
[11] Solchenbach S, Tacconis C, Gomez Martin A, Peters V, Wallisch L, Stanke A, et al. Electrolyte motion induced salt inhomogeneity – a novel aging mechanism in large-format lithium-ion cells. Energy Environ Sci 2024;17:7294–317.
[12] Bach TC, Schuster SF, Fleder E, Müller J, Brand MJ, Lorrmann H, et al. Nonlinear aging of cylindrical lithium-ion cells linked to heterogeneous compression. J Energy Storage 2016;5:212–23.
[13] Petz D, Baran V, Park J, Schökel A, Kriele A, Rebelo Kornmeier J, et al. Heterogeneity of lithium distribution in the graphite anode of 21700-Type cylindrical Li-Ion cells during degradation. Batteries 2024;10:68.
[14] Fear C, Parmananda M, Kabra V, Carter R, Love CT, Mukherjee PP. Mechanistic underpinnings of thermal gradient induced inhomogeneity in lithium plating. Energy Storage Mater 2021;35:500–11.
[15] Spingler FB, Friedrich S, Kücher S, Schmid S, López-Cruz D, Jossen A. The effects of non-uniform mechanical compression of lithium-ion cells on local Current densities and lithium plating. J Electrochem Soc 2021;168:110515.
[16] Huang J, Boles ST, Tarascon JM. Sensing as the key to battery lifetime and sustainability. Nat Sustain 2022;5:194–204.
[17] Huang J, Albero Blanquer L, Bonefacino J, Logan ER, Alves Dalla Corte D, Delacourt C, et al. Operando decoding of chemical and thermal events in commercial Na(Li)-ion cells via optical sensors. Nat Energy 2020;5:674–83.
[18] Alphen C, Forero-Saboya J, Foix D, Zhang L, Abou-Rjeily J, Mouravieff C, et al. Analyses of electrode–electrolyte interactions in commercial layered Oxide/Hard carbon Na-Ion cells via optical sensors. Adv Energy Mater 2025;15:e03527.
[19] Albero Blanquer L, Marchini F, Seitz JR, Daher N, Bétermier F, Huang J, et al. Optical sensors for operando stress monitoring in lithium-based batteries containing solid-state or liquid electrolytes. Nat Commun 2022;13:1–14.
[20] Kiran Kumar V, Ghosh S, Naresh V, al, Yan G, Dugas R, et al. Operando entropy profiling of sodium-ion batteries via optical fiber sensing for thermal management and ageing monitoring. J Electrochem Soc 2024;171:030516.
[21] Ganguli A, Saha B, Raghavan A, Kiesel P, Arakaki K, Schuh A, et al. Embedded fiber-optic sensing for accurate internal monitoring of cell state in advanced battery management systems part 2: internal cell signals and utility for state estimation. J Power Sources 2017;341:474–82.
[22] Liu F, Lu W, Huang J, Pimenta V, Boles S, Demir-Cakan R, et al. Detangling electrolyte chemical dynamics in lithium sulfur batteries by operando monitoring with optical resonance combs. Nat Commun 2023;14:1–12.
[23] Huang J, Han X, Liu F, Gervillié C, Blanquer LA, Guo T, et al. Monitoring battery electrolyte chemistry via in-operando tilted fiber Bragg grating sensors. Energy Environ Sci 2021;14:6464–75.
[24] Choi YJ, Choi J Bin, Im JS, Kim JH. Effect of porosity in activated carbon supports for silicon-based lithium-ion batteries (LIBs). ACS Omega 2023;8:19772–80.
[25] Chae S, Ko M, Kim K, Ahn K, Cho J. Confronting Issues of the Practical Implementation of Si Anode in High-Energy Lithium-Ion Batteries. Joule 2017;1:47–60.
[26] Rynearson L, Rodrigo ND, Jayawardana C, al, Graf M, Reuter L, et al. Perspective—Structure and stability of the solid electrolyte interphase on silicon anodes of lithium-ion batteries. J Electrochem Soc 2021;168:030521.
[27] Butler EJ, Kowalski N, Jager J, Johnson MB, Harlow JE, Metzger M, et al. Quantifying electrolyte motion in cylindrical Li-Ion cells using rotational inertia measurements. J Electrochem Soc 2025;172:060526.
[28] Wang L, Duan X, Liu B, Li QM, Yin S, Xu J. Deformation and failure behaviors of anode in lithium-ion batteries: model and mechanism. J Power Sources 2020;448:227468.
[29] Jung R, Metzger M, Haering D, Solchenbach S, Marino C, Tsiouvaras N, et al. Consumption of fluoroethylene Carbonate (FEC) on Si-C composite electrodes for Li-Ion batteries. J Electrochem Soc 2016;163:A1705–16.
[30] Han S, Jeong W, Kang R, Kim M, et al. Tailored electrolyte additive design for suppressing irreversibility in dry-processed anodes and enhancing electrochemical stability in full-cells. EES Batteries 2025;1:1267–78.